Medical Physics
The International Journal of Medical Physics Research and Practice

CNR considerations for rapid real-time MRI tumor tracking in radiotherapy hybrid devices: Effects of B0 field strength

K. Wachowicz, N. De Zanche, E. Yip, V. Volotovskyy, and B. G. Fallone

Citation: Medical Physics **43**, 4903 (2016); doi: 10.1118/1.4959542
View online: http://dx.doi.org/10.1118/1.4959542
View Table of Contents: http://scitation.aip.org/content/aapm/journal/medphys/43/8?ver=pdfcov
Published by the American Association of Physicists in Medicine

Articles you may be interested in

Characterizing spatiotemporal information loss in sparse-sampling-based dynamic MRI for monitoring respiration-induced tumor motion in radiotherapy
Med. Phys. **43**, 2807 (2016); 10.1118/1.4948684

Longitudinal diffusion MRI for treatment response assessment: Preliminary experience using an MRI-guided tri-cobalt 60 radiotherapy system
Med. Phys. **43**, 1369 (2016); 10.1118/1.4942381

A framework for the correction of slow physiological drifts during MR-guided HIFU therapies: Proof of concept
Med. Phys. **42**, 4137 (2015); 10.1118/1.4922403

Three-dimensional liver motion tracking using real-time two-dimensional MRI
Med. Phys. **41**, 042302 (2014); 10.1118/1.4867859

4D tumor centroid tracking using orthogonal 2D dynamic MRI: Implications for radiotherapy planning
Med. Phys. **40**, 091712 (2013); 10.1118/1.4818656

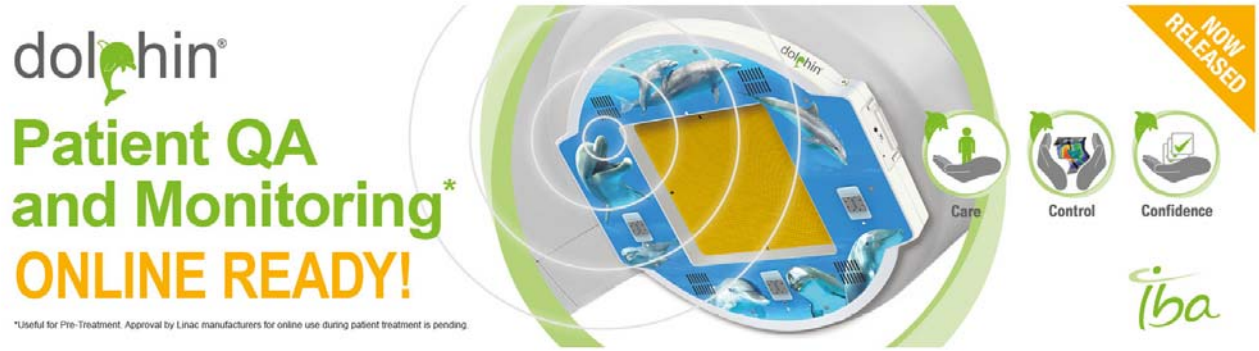

CrossMark

CNR considerations for rapid real-time MRI tumor tracking in radiotherapy hybrid devices: Effects of B_0 field strength

K. Wachowicz,[a] N. De Zanche, and E. Yip
Division of Medical Physics, Department of Oncology, University of Alberta, Cross Cancer Institute, 11560 University Avenue, Edmonton, Alberta T6G 1Z2, Canada

V. Volotovskyy
Cross Cancer Institute, Alberta Health Services, 11560 University Avenue, Edmonton, Alberta T6G 1Z2, Canada

B. G. Fallone
Department of Medical Physics, Cross Cancer Institute, 11560 University Avenue, Edmonton, Alberta T6G 1Z2, Canada and Departments of Oncology and Physics, University of Alberta, 11560 University Avenue, Edmonton, Alberta T6G 1Z2, Canada

(Received 23 February 2016; revised 8 July 2016; accepted for publication 12 July 2016; published 1 August 2016)

Purpose: This work examines the subject of contrast-to-noise ratio (CNR), specifically between tumor and tissue background, and its dependence on the MRI field strength, B_0. This examination is motivated by the recent interest and developments in MRI/radiotherapy hybrids where real-time imaging can be used to guide treatment beams. The ability to distinguish a tumor from background tissue is of primary importance in this field, and this work seeks to elucidate the complex relationship between the CNR and B_0 that is too often assumed to be purely linear.
Methods: Experimentally based models of B_0-dependant relaxation for various tumor and normal tissues from the literature were used in conjunction with signal equations for MR sequences suitable for rapid real-time imaging to develop field-dependent predictions for CNR. These CNR models were developed for liver, lung, breast, glioma, and kidney tumors for spoiled gradient-echo, balanced steady-state free precession (bSSFP), and single-shot half-Fourier fast spin echo sequences.
Results: Due to the pattern in which the relaxation properties of tissues are found to vary over B_0 field (specifically the T_1 time), there was always an improved CNR at lower fields compared to linear dependency. Further, in some tumor sites, the CNR at lower fields was found to be comparable to, or sometimes higher than those at higher fields (i.e., bSSFP CNR for glioma, kidney, and liver tumors).
Conclusions: In terms of CNR, lower B_0 fields have been shown to perform as well or better than higher fields for some tumor sites due to superior T_1 contrast. In other sites this effect was less pronounced, reversing the CNR advantage. This complex relationship between CNR and B_0 reveals both low and high magnetic fields as viable options for tumor tracking in MRI/radiotherapy hybrids.
© 2016 American Association of Physicists in Medicine. [http://dx.doi.org/10.1118/1.4959542]

Key words: MRI, linac, radiotherapy, CNR, optimal magnetic field, B_0

1. INTRODUCTION

It has been established for many years that the signal-to-noise ratio (SNR) in a well-designed MR system is roughly proportional to the strength of the polarizing magnet, B_0.[1] This assumes that the system is body-noise dominated, which is a reasonable assumption for current clinical fields and human *in vivo* imaging dimensions. Importantly, this SNR trend only considers the raw available signal after equivalent excitations and ignores the effects of relaxation which vary substantially with B_0. While these variations have been known for decades to have a profound impact on the utility of the resultant imaging, their occasionally counterintuitive nature with respect to the linear SNR relationship mentioned earlier makes them worth highlighting in the present work. This is especially true given the renewed interest in the use of low-field MR units for applications such as interventional systems, low-cost imaging, or hybrid radiotherapy devices for setup and real-time guidance purposes. This last application is the focus of this work.

It is clear that not SNR alone allows the visual or automated differentiation of tissue types. Indeed, an image with no noise whatsoever would be unable to facilitate this differentiation if the signal levels of the two tissues in question are too similar. As such, the much more appropriate metric for assessing this function is the difference in signal (or contrast) and its ratio to noise (CNR). Unlike the monotonic increase in raw signal strength with field, this contrast is heavily dependent on the relaxation properties of the tissues in question (i.e., T_1, T_2, and T_2^*), properties which in some circumstances can completely overcome any advantage that a larger B_0 may be expected to bring. This work is intended to highlight that CNR of adjacent tissues, and in particular, tumor tissue versus healthy background tissue, does not respond to a B_0 field in the linear

manner that on first assumptions one might be inclined to expect. This has implications regarding the choice of field strength for MRI-radiotherapy hybrids, complementing other considerations such as cost, dose accuracy, and siting.

There are currently a number of proposed MRI-radiotherapy hybrid designs, ranging in a B_0 field between 0.35 and 1.5 T.[2–4] While in the clinical diagnostic market, the field strength predominantly converged on 1.5 T decades ago, there are additional concerns when used with simultaneous radiotherapy that complicate this choice. For one, unlike the case of diagnostic imaging, geometric accuracy is the fundamental concern. In this respect, a reduced B_0 will lead to fewer geometric distortions resulting from the magnetic susceptibility variations. These variations naturally occur within tissue, and in particular, between tissue and implanted materials. The magnetic field arising from these variations increases at least linearly with B_0 and is thus less of a concern at low field.[5] It has also been suggested that the dose delivery of radiation will be complicated by increased field through the curling of mobile electrons within a strong magnetic field (particularly when the radiation beam is perpendicular to the field), leading to local regions of hot or cold dose surrounding air tissue interfaces.[6] Naturally, the higher the B_0 field, the more pronounced this effect on electron trajectories and the resulting dosimetric implications. However, as discussed before, the rough proportionality of SNR with field is a large incentive to maintain a higher B_0. Being that the MR-radiotherapy hybrid is in its infancy, it is unknown what, if any, optimal B_0 will eventually be converged upon. Considering that SNR will certainly be a large factor in this discussion, this work examines the issue of CNR from the perspective of real-time tumor tracking, using established pulse-sequence specific signal models and published tumor and background tissue MR relaxation rates.

TABLE I. Summary of Q measurements on the unloaded Helmholtz resonator and loaded with the head of five healthy volunteers (V1–V5). Nominal capacitance values used to tune the resonator's uniform mode to the different frequencies are also listed.

Frequency (MHz)	9.80	20.6	64.6	95.5
Capacitance (nom) (pF)	1500	360	33	15
Unloaded Q	470	600	250	230
Loaded Q (V1)	177.5	103.5	26.25	18
Loaded Q (V2)	177.5	107	28.1	19
Loaded Q (V3)	162.5	95.5	24.75	17
Loaded Q (V4)	177.5	113	26.75	18
Loaded Q (V5)	177.5	111	29.75	20

2. METHODS

2.A. Experimental assessment and modeling of field-dependent noise

As alluded to in the Introduction, the CNR of adjacent tissues depends on B_0 due to the field-dependency of tissue-specific relaxation properties and noise level, both of which must be modeled for this work. Without a proper noise model, it would be easy to over- or under-estimate the CNR, especially at frequency extremes. For example, there are greater noise

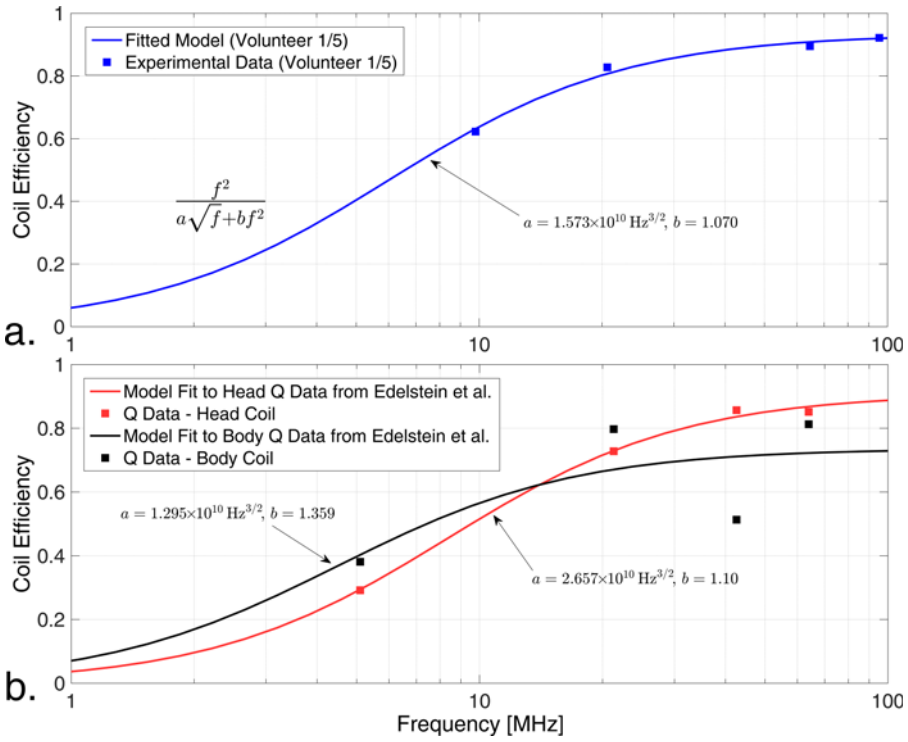

FIG. 1. (a) Measured and fitted efficiency of the Helmholtz resonator as a function of frequency for one volunteer using a model updated to include radiative losses. The fitted model parameters (a and b) are shown for this volunteer. An average of these parameter values for all five volunteers was used for subsequent analysis. (b) The same coil efficiency model as in (a) applied to data from previously published data (Ref. 7) for comparison.

TABLE II. T_1 modeling parameters and T_2 values taken from Bottomley *et al.* (Ref. 25) for use in CNR predictions. A range of spin density contrasts were imposed to reveal trends with, or robustness to differences in ρ_0. The ρ_0 values used are also summarized in this table.

	T_1 model parameters					T_1 model parameters			
Tumor tissue	A	B	T_2 (ms)	Evaluated ρ_0 values	Background tissue	A	B	T_2 (ms)	Assumed ρ_0
Liver, miscellaneous	8.23×10^{-2}	0.1334	84	0.75, ±5%, ±10%	Liver, normal	5.34×10^{-4}	0.3799	43	0.75
Lung, miscellaneous	6.77×10^{-4}	0.3954	68	0.75, ±5%	Lung, normal	4.07×10^{-3}	0.2958	79	0.29
Breast, miscellaneous	8.46×10^{-4}	0.3923	80	0.75, ±5%	Breast, fibrous	4.55×10^{-4}	0.4203	49	0.75
Kidney, miscellaneous	0.107	0.1189	83	0.75, ±5%, ±10%	Kidney, normal	7.45×10^{-3}	0.2488	58	0.75
Glioma	0.273	0.0698	111	0.75, ±5%, ±10%	White matter	1.52×10^{-3}	0.3477	92	0.75

contributions from the coil conductors at lower frequencies. Thus if a simple linear model was assumed ($SD_{Noise} \propto f$), the CNR at low fields would be over-estimated. This section addresses the development of a realistic noise model based on bench measurements on a test coil over a range of frequencies. The test coil consists of a head-sized Helmholtz resonator (two 23-cm-diameter rings separated by 11.5 cm) constructed of 3.2-mm-diameter copper tubing. While unsuitable for imaging anatomy that is likely to be treated using real-time tracking, this size was chosen because coils with a larger field of view would result in a lower proportion of noise originating from the coil, potentially overestimating the CNR.

The noise model derived from this work was based on frequency-dependent quality factor (Q) measurements, and consequently coil efficiency, which directly influences the resulting SNR.[7] The model fitted to these varying efficiencies is applicable to the reception mode of all coils, whether receive-only or transmit/receive. To obtain the Qs, the resonator's uniform (lower-frequency) mode was tuned to four separate frequencies (9.80, 20.6, 64.6, and 95.5 MHz) to investigate variations in detection efficiency. Bench measurements were made using a network analyzer in S_{21} mode and weak coupling using two-cm-diameter shielded loop probes. At each frequency, the Q was measured with the coil unloaded and loaded with the head of five healthy volunteers. These data are summarized in Table I.

Coil efficiency, η, describes the degradation in SNR relative to its intrinsic value and is calculated from the Q values according to Eq. (9.11) of Mansfield and Morris.[8] The behavior as a function of frequency was characterized by

$$\eta = \left(1 - \frac{Q_{\text{load}}(f)}{Q_{\text{unload}}(f)}\right) = \frac{\beta f^2}{\alpha\sqrt{f} + \beta f^2 + \kappa f^2} = \frac{f^2}{a\sqrt{f} + bf^2}, \quad (1)$$

which was obtained similarly to Eq. (9.7) of Ref. 8, but included loss resistance contributions due to radiation. The coil resistance in Ref. 8, R_t, was modeled here as a series combination of radiation losses ($R_{\text{rad}} = \kappa f^2$, using the short dipole approximation[9]) and ohmic coil losses $\left(R_{\text{coil}} = \alpha\sqrt{f}\right)$. The total loaded resistance is then a series combination of R_t and sample resistance $(R_S = \beta f^2)$. The additional radiative loss accounts for the observed efficiency values which approach a limit that is less than one at high frequencies [Fig. 1(a)]. Equation parameters a and b were obtained from the measured data for each volunteer by least-squares fitting using the Microsoft Excel 2010 GRG nonlinear solver. As a comparison, these parameters were also fitted [Fig. 1(b)] for published loaded and unloaded Q measurements for a head coil and a body coil.[7]

Mean parameter values obtained by averaging across the five volunteers are used to predict the SNR according to [Eq. (10) of Ref. 7],

$$\text{SNR} = \left(\sqrt{\eta} \cdot \text{iSNR}\right) \propto \left(\frac{f}{\sqrt{a\sqrt{f} + bf^2}} \cdot f\right), \quad (2)$$

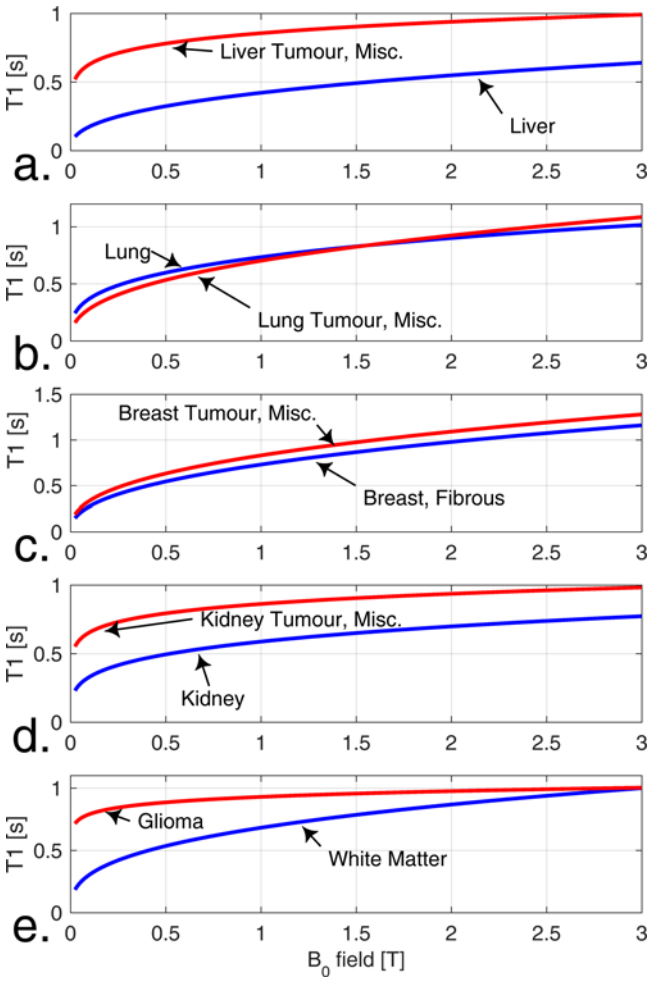

FIG. 2. Fitted T_1 models as a function of field strength, B_0, as taken from Bottomley *et al.* (Ref. 25). (a) $T_1(B_0)$ data derived from tabulated normal and tumor tissues pertaining to liver, (b) lung, (c) breast, (d) kidney, and (e) brain (white matter and glioma).

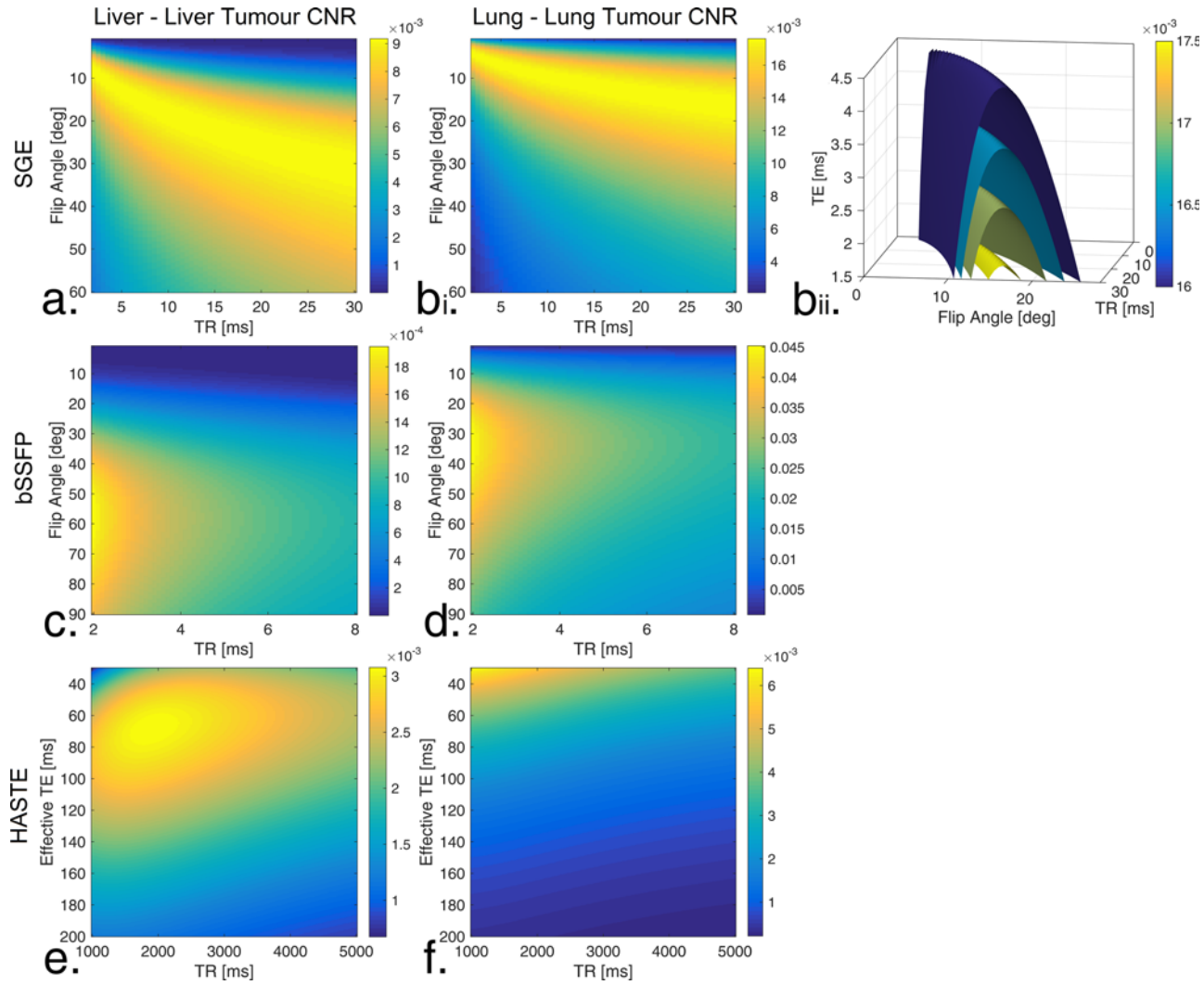

FIG. 3. Examples of parameter spaces [argument of Eq. (10)] calculated at 1 T, displayed over flip angle/effective TE and TR for liver [(a), (c), and (e)] and lung [(b), (d), and (f)]. SGE, bSSFP, and HASTE CNR maps are shown for each site (rows). In the case of SGE lung (b), an extra dimension examining the effect of TE was included (given the relatively short T_2 of lung parenchyma). The effect of all three parameters on the CNR map is shown in the surface contours of (bii). Panel (bi) illustrates this same case but with TE set to the minimal range value of 1.5 ms.

where the intrinsic SNR (iSNR) is assumed to be proportional to the square of the frequency (due to thermal polarization and Faraday induction) divided by the square root of the sample resistance (Johnson noise voltage). Although the proportionality is similar to the familiar Eq. (9) of Ref. 7, it also includes the effects of radiation resistance at higher frequencies as discussed above. The standard deviation of the noise can be easily extracted by normalizing the signal level (proportional to the square of the frequency, as above) and inverting the expression,

$$\mathrm{SD}_{\mathrm{Noise}}(f) \propto \sqrt{a\sqrt{f} + bf^2}. \tag{3}$$

A trivial substitution ($f = \gamma B_0$) then yields the field-dependent SNR relationship required in the CNR characterizations as derived in the following Subsecs. 2.B–2.C:

$$\mathrm{SD}_{\mathrm{Noise}}(B_0) \propto \sqrt{\gamma^{-3/2} a\sqrt{B_0} + bB_0^2}. \tag{4}$$

2.B. Sequences

Three rapid, clinically relevant pulse sequences suitable for real-time imaging were evaluated in this work: a spoiled gradient-echo sequence (SGE), a balanced steady-state free precession sequence (bSSFP), and a half-Fourier single-shot fast spin echo (HASTE) sequence. These sequences are important clinically, and of particular importance for the real-time tumor tracking application, can be acquired with relatively high speed.[10] SGE and bSSFP are not subject to the blurring or distortion associated with single-shot EPI acquisitions (hence their use in cardiac imaging)[11] and have a relatively large amount of signal for image generation (due to their steady-state signal available over repeated short TR intervals) (Ref. 12, Chapter 14). The HASTE sequence, being spin-refocused at each readout, is not subject to the ubiquitous B_0 distortion of the EPI readout (although there is some degree of blurring due to the T_2 modulation of available signal over the prolonged k-space acquisition).[13] Thus these are appropriate sequence examples for CNR evaluations in this

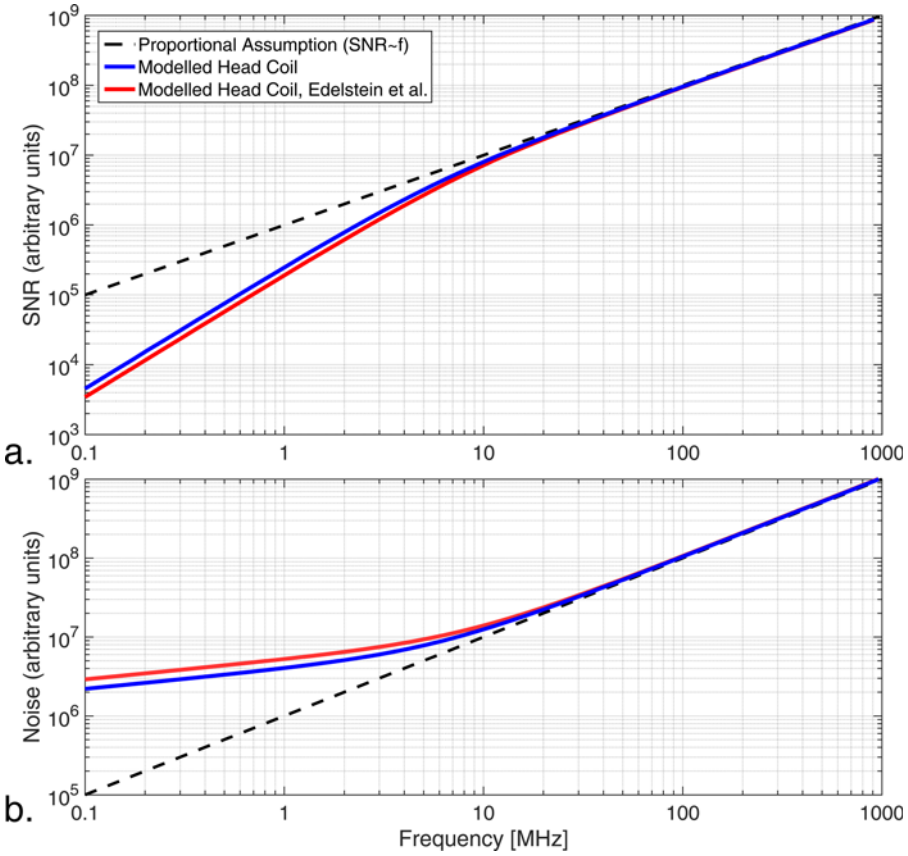

FIG. 4. (a) Modeled SNR of our head-sized Helmholtz resonator, based on experimental Q measurements. Using the same model, SNR predictions of the head coil measurements published by Edelstein *et al.* (Ref. 7) are also displayed. Note that for coil dimensions of this order, the SNR is essentially linear with respect to resonant frequency above a threshold of approximately 50 MHz, but begins to deviate sizably from this trend below roughly 10 MHz. (b) Corresponding noise standard deviation predicted by the same model.

work on real-time tumor tracking. The bSSFP sequence can be implemented to achieve frame rates of about 4/s as required for targeting tumors with cyclic motion correlated with breathing (based on recommendations given in the AAPM Task Group 76 report).[14,15] While the bSSFP sequence is limited by banding artifacts to having a short TR, SGE is amenable to use with longer TRs which could be suitable for tracking tumors that are not subject to respiratory motion but may be subject to displacement over a radiotherapy treatment interval (several minutes). Single-shot techniques, such as HASTE, are rapidly acquired but require time for signal recovery between excitations. As such, it is generally incapable of subsecond implementations but could fill a role in tumor sites with slower motions of a longer duration (relative to the duration of treatment).

The signal equation for the SGE can be written as[12]

$$S_{\mathrm{SGE}}(B_0,\mathrm{TR},\theta,\rho_0,\mathrm{TE}) \propto {B_0}^2\rho_0 \sin\theta \frac{1-\mathrm{e}^{-\mathrm{TR}/T_1(B_0)}}{1-\mathrm{e}^{-\mathrm{TR}/T_1(B_0)}\cos\theta}\mathrm{e}^{-\mathrm{TE}/{T_2}^*(B_0)}. \quad (5)$$

Note that although ${T_2}^*$ is a variable in this equation, for the simulations it was assumed that TE was kept short enough to disregard the ${T_2}^*$ decay term. An exception was made in the case of normal lung tissue, for which the ${T_2}^*$ is quite short due to magnetic susceptibility effects of the air/tissue interfaces that pervade the lung parenchyma. Experimental values at 0.2, 1.5, and 3.0 T were found in the literature[16,17] and were used to obtain a simple linear model for ${R_2}^* = 1/{T_2}^*$ versus B_0,

$${R_2}^*{}_{\mathrm{lung}} = 0.012\,\mathrm{ms}^{-1} + 4.4\,\mathrm{ms}^{-1}T^{-1}\times B_0. \quad (6)$$

Second, the bSSFP sequence can be described with the following signal equation:[12]

$$S_{\mathrm{bSSFP,alt}}(B_0,\mathrm{TR},\theta,\rho_0) \propto {B_0}^2\rho_0 \sin\theta \times \frac{[1-E_1(B_0)]\cdot[E_2(B_0)]^{1/2}}{1-[E_1(B_0)-E_2(B_0)]\cos\theta-[E_1(B_0)\cdot E_2(B_0)]}, \quad (7)$$

where,

$$E_1(B_0) = \mathrm{e}^{-\mathrm{TR}/T_1(B_0)}$$
$$E_2(B_0) = \mathrm{e}^{-\mathrm{TR}/T_2(B_0)}. \quad (8)$$

Here, the alternating-phase signal equation was chosen [indicated by the subscript alt in Eq. (7)], as it in general generates the most favorable signal levels at the resonant frequency.

Finally, the image signal corresponding to the HASTE sequence can be represented as

$$S_{\mathrm{HASTE}}(B_0,\mathrm{TR},\rho_0,\mathrm{TE_{Eff}}) \propto {B_0}^2\rho_0\left(1-\mathrm{e}^{-\mathrm{TR}/T_1(B_0)}\right)\mathrm{e}^{-\mathrm{TE_{Eff}}/T_2(B_0)}, \quad (9)$$

where the subscript after "TE" identifies this parameter as an effective one, based on the time at which the central line of k-space is sampled. Note that no dependency on flip angle is present due to the assumption of a 90° excitation pulse. While it is generally considered a sequence dominated by T_2 weighting, the incentive to reduce the TR to increase the acquired image frame rate will generate a certain degree of T_1 weighting, captured by the term in parentheses.

In all equations, the ${B_0}^2\rho_0$ terms represent the maximum magnetization, with ρ_0 representing spin density (for the following work, this spin density is normalized to that of water). Finally, one will note that the effect of matrix and voxel size has been excluded from all the signal equations. This represents an implicit assumption that the voxel size is constant across all imaging fields for the sake of simplicity and easy comparison.

2.C. CNR estimates

The signal levels described in Eqs. (5), (7), and (9) vary on the basis of the B_0 field-dependent relaxation rates, as well as sequence timings and flip angle, θ. Therefore, to allow for fair comparison between different B_0 fields, an optimization process was carried out at each B_0 field under consideration to obtain the optimal combination of TR, θ or $\mathrm{TE_{Eff}}$, and TE in the case of lung SGE that generates the maximal CNR between the tumor and background tissues. The resulting maximal predictions of CNR efficiency can be summarized by the following equation:

$$\mathrm{CNR_{eff}}(B_0) \propto \max_{\mathrm{TR},(\theta),(\mathrm{TE_{Eff}})(\mathrm{TE})} \left(\mathrm{abs} \left[\begin{array}{r} S_{\mathrm{Tumour}}(B_0,TR,(\theta),(\mathrm{TE_{Eff}}),\rho_0,(\mathrm{TE})) - \\ S_{\mathrm{Normal}}(B_0,\mathrm{TR},(\theta),(\mathrm{TE_{Eff}}),\rho_0,(\mathrm{TE})) \end{array} \right] \times \frac{1}{\mathrm{SD_{Noise}}(B_0)} \times \frac{1}{\sqrt{\mathrm{TR}}} \right). \quad (10)$$

The first factor in this equation represents the absolute signal difference between the two tissue types. The second factor divides the resulting contrast by the modeled, field-dependent standard deviation of the noise as described by Eq. (4). Finally, the third factor scales this resultant CNR value to reflect the consequence of TR on noise-reduction due to averaging within a constant imaging duration (hence CNR efficiency). Given a constant imaging duration, T_{dur}, and identical k-space readouts, the number of signal averages can be taken to be $N_{\mathrm{Ave}} = T_{\mathrm{dur}}/(N_{\mathrm{TRperAve}} \cdot \mathrm{TR})$. Since the standard deviation of the averaged noise can be represented as $(\mathrm{SD_{Noise}}/\sqrt{N_{\mathrm{Ave}}}) \propto \mathrm{SD_{Noise}}\sqrt{\mathrm{TR}}$.[18] Consequently, the term $\sqrt{\mathrm{TR}}$ must appear in the denominator alongside $\mathrm{SD_{Noise}}(B_0)$ to control for a constant imaging time in these comparisons. This normalization allows a straightforward and meaningful comparison of CNR between different scenarios. One need not consider factors such as sampling frequency and matrix parameters since their selection is not necessarily dependent on field strength, and thus they can be considered a constant for the sake of comparison.

The image contrast one can obtain from spin-density weighted imaging alone is limited.[19] It is for this reason that the vast majority of clinical imaging utilizes relaxation differences as the primary contrast mechanism. Regarding proton density differences between tumor and normal tissue, researchers have often found that the water content of tumor tissues is slightly elevated over that of the normal.[20,21] This observation is not valid in general, however, and can be shown to vary within tumor types.[22] To investigate the robustness of the simulated CNR curves with respect to proton density variation, curves were generated under three scenarios: tumor spin density elevated over background by 5%, equal to background, and below background by 5%. In the cases where the pattern of change due to spin density variation is complicated, extra examinations at $\rho_0 \pm 10\%$ were included. Given that the effect of proton density on relative CNR through B_0 will be solely dependent on the ratio of proton densities between tumor and background [this can be deduced from the fact that proton density is a scalar constant applied to the signal expressions in Eq. (10)], normal tissues (with the exception of lung) were arbitrarily assigned a nominal value of 0.75. The proton density ratios were then established by assigning tumor proton densities to a range of values above and below 0.75, as can be seen in Table II. This method was chosen due to the difficulty the authors encountered in finding reliable and consistent proton density values, particularly for tumor tissues. It was felt that more benefits for the reader would come from exploring a range of proton density ratios between tumor and normal tissue, rather than just basing our results on potentially inaccurate numbers for which the authors had little confidence. It is important to note, however, that all the contrast variations with magnetic field will originate from relaxation properties in this model.

The only exception to the above spin density assignments was bulk normal lung tissue, which has very low density due to the presence of air. Lung spin density has been reported to have an experimental value of 0.29 ± 0.08.[23] (This is consistent with mass density measurements which have reported a density of 0.26.[24]) Thus lung spin density was assigned to $\rho_0 = 0.29$ for this exercise. Data for $T_1(B_0)$ and T_2 were taken from Bottomley *et al.*[25] This valuable source assessed and modeled the variation of measured relaxation values quoted across the literature for a wide range of low B_0 fields—fields that have largely fallen out of widespread

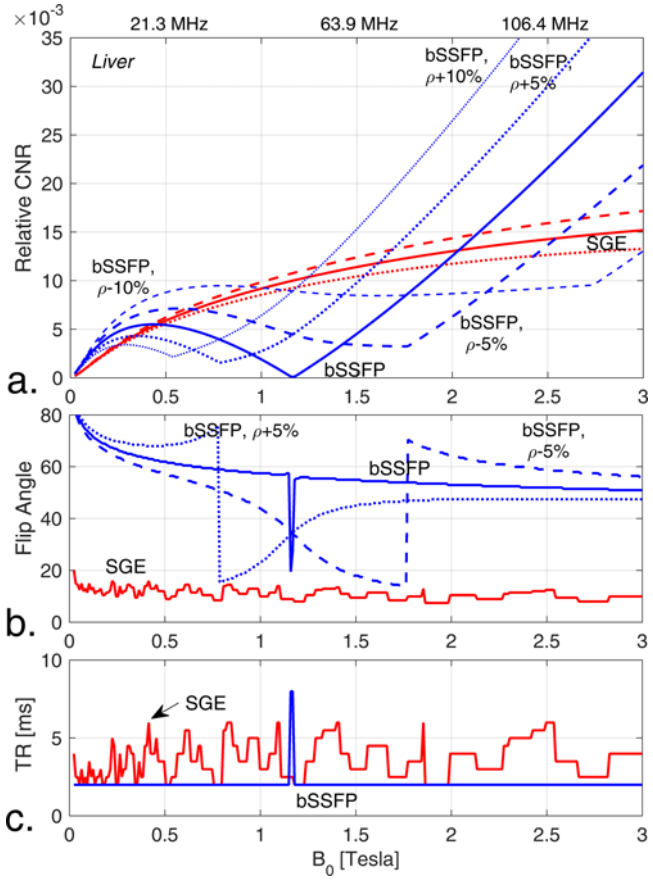

FIG. 5. (a) Predictions of maximal CNR for liver tumors set against normal liver tissue [using relaxation parameters as tabulated by Bottomley *et al.* (Ref. 25)] generated from the models of the spoiled gradient-echo (SGE) sequence and bSSFP. (b) The optimal flip angle associated with the CNR plots in (a) as selected by the optimization routine. (c) The optimal TR associated with the CNR plots in (a) as selected by the optimization routine. Note that for bSSFP, the TR giving optimal CNR was found at the extreme limits of the range. (Dashed lines and dotted lines represent decreases and increases in tumor proton density, respectively.)

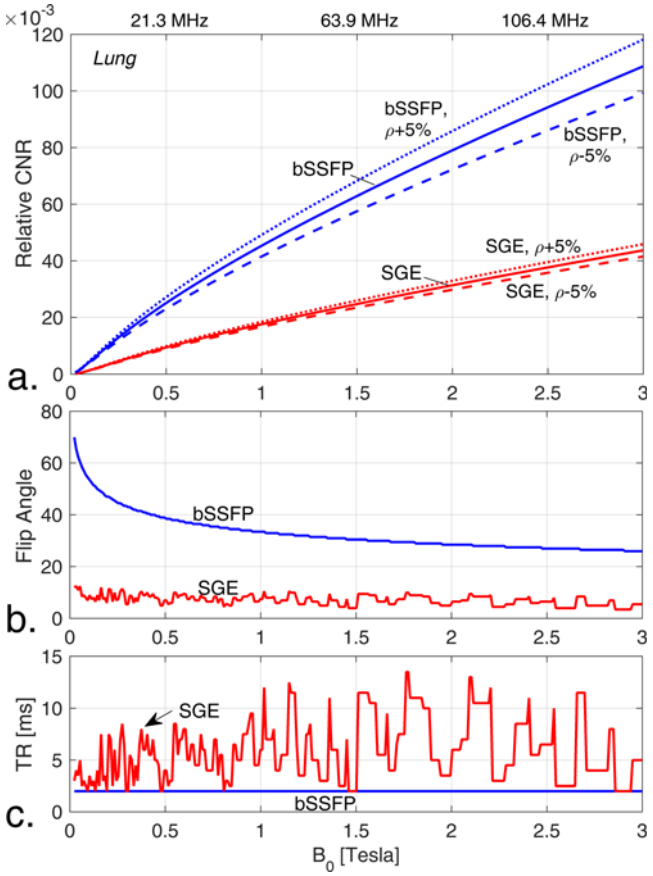

FIG. 6. (a) Predictions of maximal CNR for lung tumors set against normal lung tissue [using relaxation parameters as tabulated by Bottomley *et al.* (Ref. 25)] generated from the models of the spoiled gradient-echo (SGE) sequence and bSSFP. (b) The optimal flip angle associated with the CNR plots in (a) as selected by the optimization routine. (c) The optimal TR associated with the CNR plots in (a) as selected by the optimization routine. Note that for bSSFP, the TR giving optimal CNR was found at the minimum limit of the range (2 ms). (Dashed lines and dotted lines represent decreases and increases in tumor proton density, respectively.)

clinical use. This aforementioned modeling characterized the T_1 dispersion using an expression with two tissue-specific parameters ($T_1(B_0) = A[f(B_0)]^B$, where f represents frequency in Hz, and the resulting T_1 is in seconds), and supplied the best-fit parameters for a variety of tissues. This current work utilizes these published parameters and models to investigate B_0-related trends in CNR. The resulting $T_1(B_0)$ curves for the tissues used in this work are displayed in Fig. 2. As expected from theory and measurement,[26] the T_2 values were assumed to be approximately constant over the field range between 0.5 and 3 T (compared to T_1) and were thus entered as constants in the equations. The published parameters describing the $T_1(B_0)$ relationship, and the T_2 values that were taken from Bottomley *et al.* are listed in Table II. It should be noted that diagnostic MRI will frequently utilize gadolinium-based contrast agents to enhance the contrast between tumor structures and background, effectively altering the values displayed in Table II and Fig. 2. However, given that real-time tracking during radiotherapy will employ many repeated scans over the course of a treatment, a conservative approach that optimizes contrast without the administration of gadolinium agents would be preferred for the sake of patient safety. Consequently, only endogenous tissue/tumor contrast was considered in this work. However, it should be pointed out that in certain cases where tumor visualization is difficult to achieve via endogenous means, the administration of contrast may outweigh the risks.

Optimization of TR and θ (or TE_{Eff}) in Eq. (10) was performed on a one-to-one basis between each tissue/tumor pair by creating a vector of all permitted values for each variable. For SGE and bSSFP, a vector between 1° and 60° with 0.5° resolution was defined for the flip angle. The TR vector was defined to range between 2 and 8 ms or 2–30 ms with 0.5 ms resolution for bSSFP and SGE, respectively, and between 1000 and 5000 ms (25 ms resolution) for HASTE. Initially, the TR vector for SGE was extended to 500 ms with a coarser resolution. However, in subsequent optimizations, only the lower portion of the range was found to be relevant, leading us to limit it to 30 ms. The bSSFP TR was capped at 8 ms given the propensity of that sequence to create banding artifacts due to B_0 inhomogeneity, artifacts which become

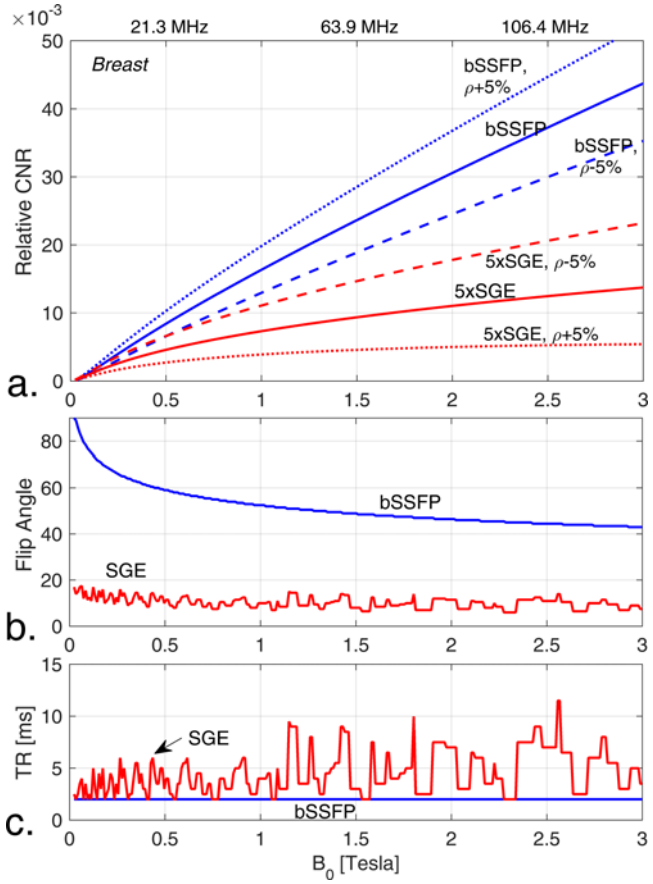

FIG. 7. (a) Predictions of maximal CNR for breast tumors set against normal fibrous breast tissue [using relaxation parameters as tabulated by Bottomley *et al.* (Ref. 25)] generated from the models of the spoiled gradient-echo (SGE) sequence and bSSFP. (b) The optimal flip angle associated with the CNR plots in (a) as selected by the optimization routine. (c) The optimal TR associated with the CNR plots in (a) as selected by the optimization routine. Note that for bSSFP, the TR giving optimal CNR was found at the minimum limit of the range (2 ms). (Dashed lines and dotted lines represent decreases and increases in tumor proton density, respectively.)

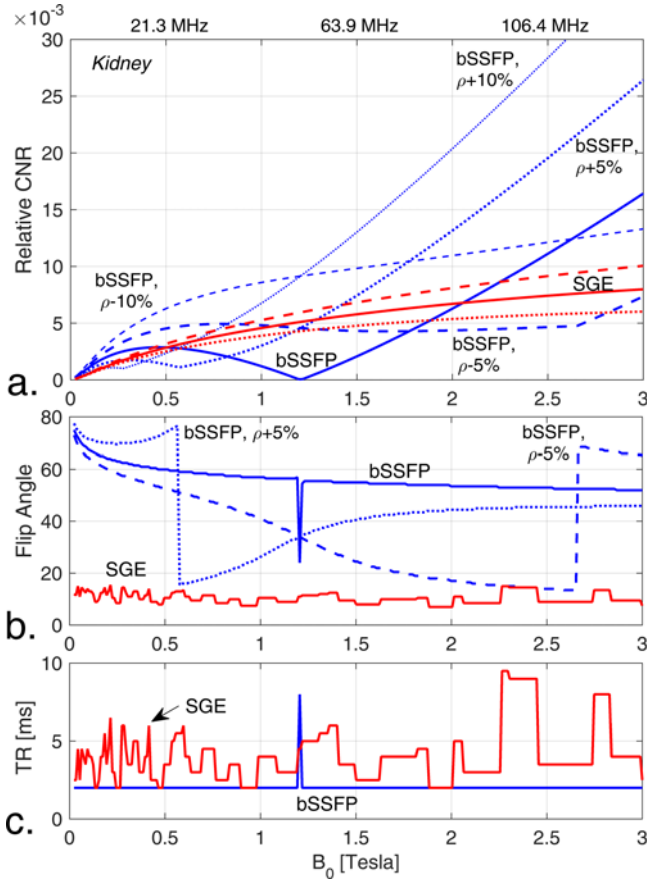

FIG. 8. (a) Predictions of maximal CNR for kidney tumors set against normal kidney tissue [using relaxation parameters as tabulated by Bottomley *et al.* (Ref. 25)] generated from the models of the spoiled gradient-echo (SGE) sequence and bSSFP. (b) The flip angle associated with the CNR plots in (a) as selected by the optimization routine. (c) The TR associated with the CNR plots in (a) as selected by the optimization routine. Note that for bSSFP, the TR giving optimal CNR was found at the extreme limits of the range. (Dashed lines and dotted lines represent decreases and increases in tumor proton density, respectively.)

continuously more severe as the TR increases. Consequently, in clinical circumstances, the TR is generally kept as short as possible. Given the limited 2D parameter spaces for most of the scenarios, Eq. (10) was calculated for all points to determine the optimal set of parameters, yielding a maximal CNR efficiency at a given B_0. (See Fig. 3, for examples of these 2D CNR efficiency maps used to identify the optimal parameter pairs.) In the case of SGE lung only, an extra vector for TE between 1.5 and 10 ms was included in the optimization, yielding a 3D optimization for every B_0 value. In all cases, this procedure was used to optimal sequence parameters for each of 300 B_0 values evenly spaced between 0.025 and 3 T.

3. RESULTS AND DISCUSSION

The fitting of the experimental Q measurements to the coil efficiency model [Eq. (1)] yielded mean parameters of $a = 1.527(\pm 0.096) \times 10^{10}$ Hz$^{3/2}$ and $b = 1.076(\pm 0.007)$, from which the field-dependency of SNR can be predicted for coils of this general geometry (Fig. 4). It is evident that above a Larmor frequency of roughly 50 MHz, a nearly proportional relationship exists between SNR and frequency with head coils. As frequency decreases below 10 MHz, the linear model increasingly overestimates SNR due to the increasing noise contributions of coil conductors. Very similar results are obtained from the head coil data from Edelstein *et al.*[7] The parameters derived from these published data [the fit is shown in Fig. 1(b)] were averaged with our own to generate the noise standard deviation described in Eq. (4) and used for our CNR predictions. These final parameters were therefore $a = 2.092 \times 10^{10}$ Hz$^{3/2}$ and $b = 1.088$. One will note that although the plots in Fig. 4 appear roughly linear over the span of currently proposed B_0 fields (0.35, 0.5, and 1.5 T),[2–4] inspection of the log–log plots will reveal a drop in SNR at the low end of this range in the order of 10%–20%. As a result, this full noise model was incorporated into our CNR predictions in order to present the results from the lower fields as accurately as possible. The body coil data of Ref. 7 were not smoothly varying and did not provide a satisfactory fit to our model.

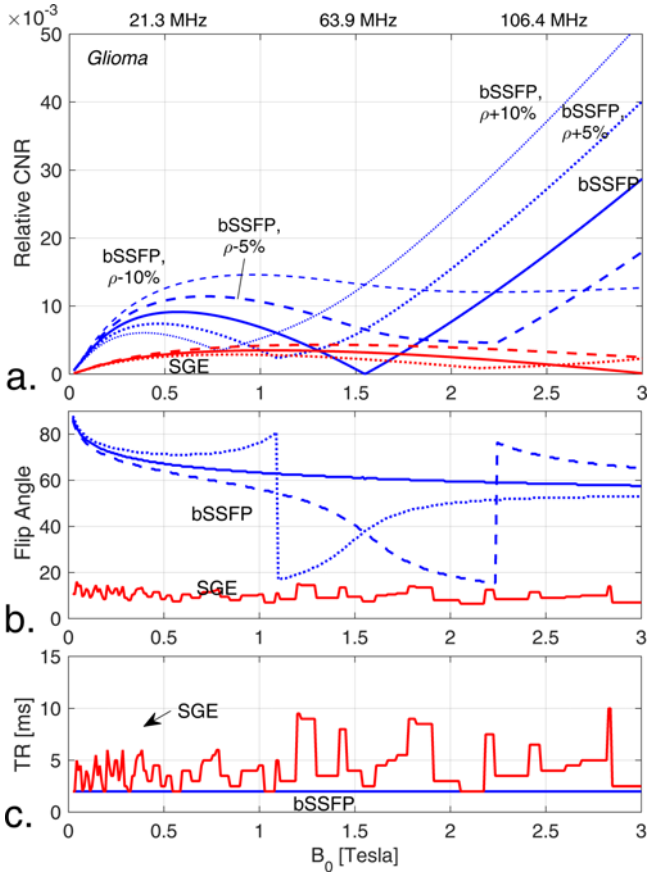

FIG. 9. (a) Predictions of maximal CNR for glioma tumors set against normal white matter [using relaxation parameters as tabulated by Bottomley *et al.* (Ref. 25)] generated from the models of the spoiled gradient-echo (SGE) sequence and bSSFP. (b) The optimal flip angle associated with the CNR plots in (a) as selected by the optimization routine. (c) The optimal TR associated with the CNR plots in (a) as selected by the optimization routine. Note that for bSSFP, the TR giving optimal CNR was found at the minimum limit of the range (2 ms). (Dashed lines and dotted lines represent decreases and increases in tumor proton density, respectively.)

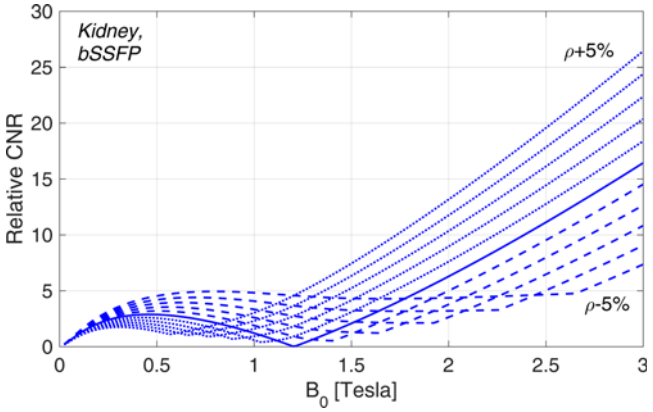

FIG. 10. Variation in CNR efficiency curves for the case of kidney tumors due to 1% interval changes in the ratio spin density (tumor to normal). This reveals how this type of pattern often seen in the bSSFP examples can be interpolated. Dashed lines represent a reduced tumor spin density with respect to normal, whereas dotted lines represent an increased one.

Nevertheless, head-sized coils are the most appropriate for this CNR evaluation, as the coil noise is more likely to dominate than in their body-sized counterparts. Indeed, head coils can be considered a worst case scenario for most clinical radiation therapy volume imaging circumstances. The use of this head-sized coil model ensures that our model-predicted CNR at low fields is not over-estimated due to potential dependencies of noise content on coil size.

Maximized CNR predictions based on Eq. (10) are illustrated between a variety of tumor types (liver, lung, breast, kidney, and glioma) and their normal background tissue for SGE and bSSFP in Figs. 5–9. They have a wide range of responses, suggesting that for optimal CNR efficiency in tumor tracking, one should set up independent protocols for each site. In most cases, the variation of curves due to spin density ratio changes (in 5% intervals) is seen as evenly spaced and relatively easy to interpolate visually. In general the patterns of change were more complex for bSSFP than SGE. The most complex example (bSSFP of kidney tumor) is further illustrated in Fig. 10, showing clearly how the pattern evolves with finer spin density ratio changes (intervals of 1%).

Let us first consider the case of SGE. It is evident that, in general, the maximum CNR increases with field strength, as expected. What is interesting, however, is that this increase is slower in general than the simplistic linear expectation. For example, liver, breast, and kidney tumors have roughly twice the CNR at 1.5 T versus 0.5 T, as opposed to the threefold increase that one might expect from a linear assumption. Further, in the case of glioma, the relaxation properties were such that its CNR with respect to white matter was fairly constant between 0.5 and 1.5 T, peaking at between 0.8 and 1.3 T, depending on the relative spin density. Since our signal model for SGE was dependent only on T_1 (except the case of lung, where the effects of T_2^* were included), this is suggestive of a greater dispersion of T_1 at lower B_0 field compensating to a greater or lesser degree for the loss of intrinsic signal at these lower fields. There are some data to support this general trend, such as Fig. 2.2 of Mansfield and Morris,[8] where a greater fractional spread of T_1 values is seen as the B_0 field is reduced. Of course, this trend is only a generalization, and there are likely some exceptions, depending on the tissue types involved.

The inclusion of TE as a CNR optimizing variable for SGE of lung (given the rapid T_2^* decay of lung parenchyma) was not found to be a significant factor in the resulting CNR. At all B_0 fields that were investigated, the optimal TE for maximal CNR was placed at the minimal value in the range (1.5 ms), despite the range extending out to 10 ms. This suggests that in this particular case, the T_1 and T_2^* contrasts are in opposition, with T_1 being dominant.

The results from bSSFP are more disparate. On the one hand, breast and lung tumors at 0.5 T were found to exceed the linear CNR assumption relative to 1.5 T by only a small margin. Fortunately, these targets have relatively high contrast in general, particularly lung, which derives a significant portion of its contrast from a large difference in spin density. Conversely, some of the other tumor examples actually showed

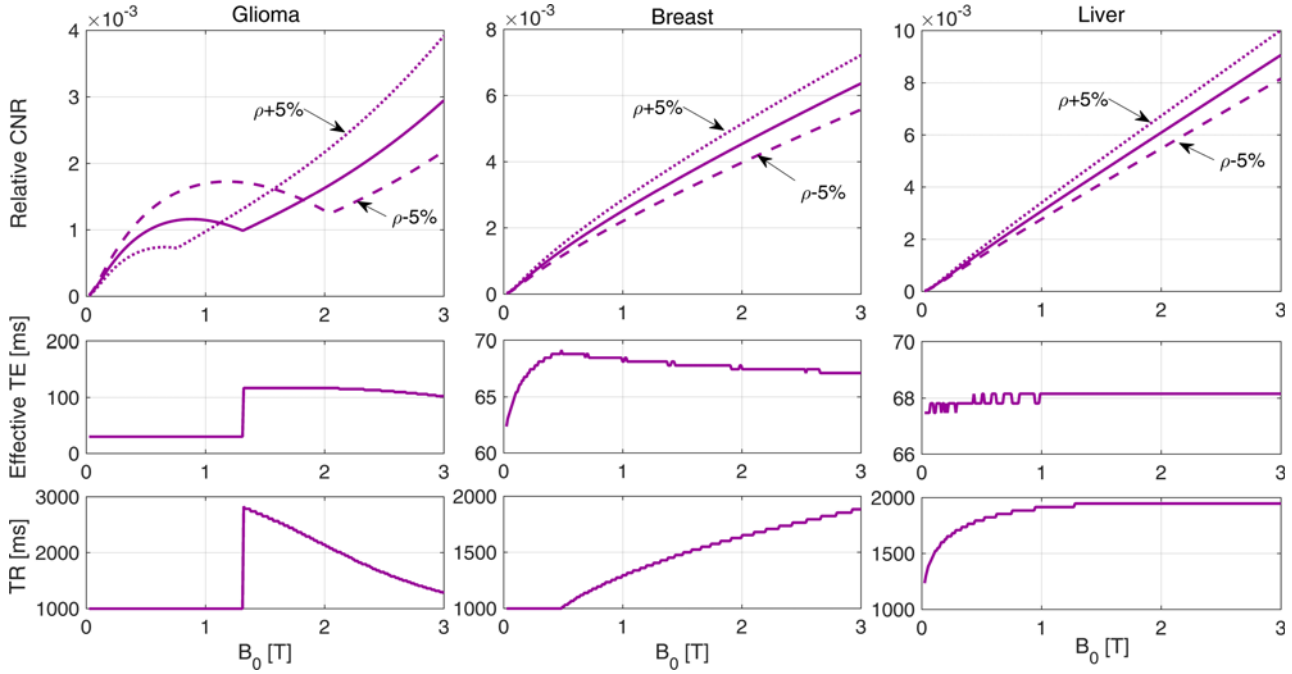

FIG. 11. Optimal HASTE CNR efficiency curves for the case of glioma vs white matter, breast tumor vs fibroglandular tissue, and liver tumor vs normal liver. Note that this optimization often included the shortening of TR which will introduce some T_1 weighting.

more favorable CNR at lower fields: the glioma tumor example indicated a peak CNR at around 0.6 T, and the kidney and liver tumors were found to have CNR levels at 0.5 T similar to, if not larger than what is seen at 1.5 T. Note that for these last two tumor types, there is a region in between 0.5 and 1.5 T, where the CNR reaches a minimum.

One will also notice that there is often a discontinuous interplay between flip angle and TR when determining maximal CNR. This can be seen occasionally for the bSSFP case in Figs. 5 and 8 and heavily in all the SGE examples. For SGE, this is due to the presence of a linear distribution of maxima of roughly uniform values across the solution space, as can be seen in Figs. 3(a) and 3(b), resulting in discontinuous jumps of the independent variables TR and θ, likely originating from their discretization. Despite this, the maximal CNR plot is completely smooth, suggesting that there is a range of TR and θ pairs at each field that would result in nearly the same CNR, a positive result given that practical or scanner restrictions may limit choices for TR or θ [i.e., for specific absorption rate (SAR) limitations]. In the case of bSSFP, the TR is usually fixed at the value of its minimal range (2 ms). Likely, the maximal CNR would be found to improve if this minimum was reduced. However, for practical hardware reasons, many clinical scanners are unable to achieve a shorter TR than this, hence its choice as a minimum. Only at times where the maximal CNR is seen to drop near 0 due to similarities in relaxation properties between the target and background tissues does this TR selection change abruptly to the maximum limit (which was set to 8 ms for reasons given in Methods). This implies that there is a weak maximum present at high TR, which becomes relevant only when the maximum at short TR fails. Such a secondary maximum can be seen in Fig. 3(c) at high TR and low flip angle. Finally, one will note that the bSSFP optimizations frequently suggest using relatively low flip angles (in the order of 20°). While this is not standard in the clinic, for the specific application of identifying a tumor from background, the signal equations are predicting that at times this will create an improved CNR efficiency.

Selected results for the HASTE sequence are shown below in Fig. 11. For most cases the CNR efficiency evolved with B_0 in a somewhat linear fashion. The cases of lung and kidney tumors (not shown) were qualitatively very similar to those of breast and liver, respectively. The breast and lung cases show a small degree of improvement over linear at low fields. However, for liver and kidney tumors, the CNR efficiency appears completely linear with B_0. The case of glioma was different in that the CNR at low field entered a different contrast regime (T_1 dominated, judging by the shorter TR and shorter effective TE), allowing the achievable CNR at 0.5 T, for example, to approach that of 1.5 T. While T_1 weighting may not be a conventional feature of HASTE imaging, here, it seems to aid in the ultimate objective of better visualizing tumor structures for tracking.

One important factor affecting CNR efficiency that was not dealt with in this work is that of SAR. To first order, SAR can be easily shown to vary quadratically with B_0 and pulse amplitude (B_1).[27] Therefore, at higher fields, sacrifices may have to be made in the form of increased repetition times or reduced (suboptimal) flip angles that reduce the achievable CNR efficiency seen in Figs. 5–9 as B_0 increases. The HASTE sequence poses an even more formidable SAR issue given that the sequence involves long chains of refocusing pulses, nominally using flip angles of 180°. However, there are multi-faceted approaches to mitigating this issue at high field, including wider, lower-amplitude pulses (sequence and hardware permitting),

reduced flip angle schemes, and parallel multi-transmit radio frequency to reduce local SAR hotspots.[28] As a result, incorporating the constraints of SAR into the CNR efficiency model would be an awkward endeavor, one that may lessen the impact of the results. Nevertheless, the impact of SAR at high fields remains and should be considered as an additional factor impacting the choice of field for real-time tracking.

The Bottomley collection and T_1 models were convenient to use and represented relaxation times sourced from a wide range of B_0 fields. However, it is important to point out that due to collection of data obtained using a variety of methodologies and tissues (including some animal models), it should be understood that the accuracy of the models is limited. As a result, the CNR efficiencies calculated in this work are primarily useful as a means to observe general trends and the manner in which CNR efficiency may vary with field strength. Further, while the results herein are based on well-established signal models, it is acknowledged that patient studies are the ultimate confirmation of CNR trends with B_0. The results of this work can provide impetus for future patient studies, particularly directed at tumor sites that were predicted to have an unexpected CNR equivalency or advantage at lower fields when compared to fields such as 1.5 T. Finally, while this work focused on relatively rapid robust sequences suitable for real-time tumor tracking, the methodology presented herein can easily be extended to cover a wide range of sequence types suitable for a broader variety of imaging purposes. This is the subject of future work.

4. CONCLUSIONS

Examination of three rapid MR sequences common in clinical imaging, including a thorough noise model, has shown that the CNR between a target tissue (i.e., tumor) and its background cannot be assumed to vary linearly with field strength. While certain sites may have a CNR trend that approaches this linearity, there are other sites (brain, kidney, liver) that generate higher-than-expected CNR at low field, which at times can exceed that achievable at a field strength of 1.5 T. Thus it seems that from a CNR point of view, the optimal magnetic field for rapid imaging of tumor structures will be dependent on pathology and sequence. These findings suggest that lower field strengths are strong candidates for real-time imaging during radiotherapy, not only because of reduced geometrical distortions but in some cases also because of better contrast.

ACKNOWLEDGMENT

The authors would like to acknowledge Alberta Innovates–Health Solutions (AIHS) for funding, and the Izaak Walton Killam Memorial Scholarship for support of E.Y.

CONFLICT OF INTEREST DISCLOSURE

The authors are affiliated with MagnetTx Oncology Solutions, of which B.G.F. is co-founder and CEO.

[a]Author to whom correspondence should be addressed. Electronic mail: keith.wachowicz@albertahealthservices.ca

[1]A. Macovski, "Noise in MRI," Magn. Reson. Med. **36**(3), 494–497 (1996).
[2]O. P. Green, S. Goddu, and S. Mutic, "Commissioning and quality assurance of the first commercial hybrid MRI-IMRT system," Med. Phys. **39**(6), 3785 (2012).
[3]B. G. Fallone, "The rotating biplanar linac–magnetic resonance imaging system," Semin. Radiat. Oncol. **24**(3), 200–202 (2014).
[4]J. J. W. Lagendijk, B. W. Raaymakers, A. J. E. Raaijmakers, J. Overweg, K. J. Brown, E. M. Kerkhof, R. W. van der Put, B. Hardemark, M. van Vulpen, and U. A. van der Heide, "MRI/linac integration," Radiother. Oncol. **86**(1), 25–29 (2008).
[5]K. Wachowicz, T. Stanescu, S. D. Thomas, and B. G. Fallone, "Implications of tissue magnetic susceptibility-related distortion on the rotating magnet in an MR-linac design," Med. Phys. **37**(4), 1714–1721 (2010).
[6]C. Kirkby, B. Murray, S. Rathee, and B. G. Fallone, "Lung dosimetry in a linac-MRI radiotherapy unit with a longitudinal magnetic field," Med. Phys. **37**(9), 4722–4732 (2010).
[7]W. A. Edelstein, G. H. Glover, C. J. Hardy, and R. W. Redington, "The intrinsic signal-to-noise ratio in NMR imaging," Magn. Reson. Med. **3**(4), 604–618 (1986).
[8]P. Mansfield and P. G. Morris, *NMR Imaging in Biomedicine: Supplement 2, Advances in Magnetic Resonance* (Academic, New York, NY, 1982).
[9]W. R. Smythe, *Static and Dynamic Electricity*, 3rd ed. (McGraw-Hill, New York, NY, 1968).
[10]J. P. Finn, K. Nael, V. Deshpande, O. Ratib, and G. Laub, "Cardiac MR imaging: State of the technology," Radiology **241**(2), 338–354 (2006).
[11]J. C. Moon, C. H. Lorenz, J. M. Francis, G. C. Smith, and D. J. Pennell, "Breath-hold FLASH and FISP cardiovascular MR imaging: Left ventricular volume differences and reproducibility," Radiology **223**(3), 789–797 (2002).
[12]M. A. Bernstein, K. F. King, and X. J. Zhou, *Handbook of MRI Pulse Sequences* (Elsevier, New York, NY, 2004).
[13]M. R. Patel, R. A. Klufas, R. A. Alberico, and R. R. Edelman, "Half-Fourier acquisition single-shot turbo spin-echo (HASTE) MR: Comparison with fast spin-echo MR in diseases of the brain," Am. J. Neuroradiol. **18**(9), 1635–1640 (1997).
[14]J. Yun, E. Yip, K. Wachowicz, S. Rathee, M. Mackenzie, D. Robinson, and B. G. Fallone, "Evaluation of a lung tumor autocontouring algorithm for intrafractional tumor tracking using low-field MRI: A phantom study," Med. Phys. **39**(3), 1481–1494 (2012).
[15]P. J. Keall, G. S. Mageras, J. M. Balter, R. S. Emery, K. M. Forster, S. B. Jiang, J. M. Kapatoes, D. A. Low, M. J. Murphy, B. R. Murray, and C. R. Ramsey, "The management of respiratory motion in radiation oncology report of AAPM Task Group 76," Med. Phys. **33**(10), 3874–3900 (2006).
[16]A. Boss, S. Schaefer, P. Martirosian, C. D. Claussen, F. Schick, and J. F. Schaefer, "Magnetic resonance imaging of lung tissue: Influence of body positioning, breathing and oxygen inhalation on signal decay using multi-echo gradient-echo sequences," Invest. Radiol. **43**(6), 433–438 (2008).
[17]J. Yu, Y. Xue, and H. K. Song, "Comparison of lung T_2^* during free-breathing at 1.5 T and 3.0 T with ultrashort echo time imaging," Magn. Reson. Med. **66**(1), 248–254 (2011).
[18]J. R. Taylor, *An Introduction to Error Analysis: The Study of Uncertainties in Physical Measurements* (University Science Books, Mill Valley, CA, 1982).
[19]Z.-P. Liang and P. C. Lauterbur, *Principles of Magnetic Resonance Imaging: A Signal Processing Perspective* (IEEE, Piscataway, NJ, 2000).
[20]D. P. Hollis, L. A. Saryan, J. C. Eggleston, and H. P. Morris, "Nuclear magnetic resonance studies of cancer. VI. Relationship among spin-lattice relaxation times, growth rate, and water content of Morris hepatomas," J. Natl. Cancer Inst. **54**(6), 1469–1472 (1975).
[21]I. C. Kiricuta and V. Simplăceanu, "Tissue water content and nuclear magnetic resonance in normal and tumor tissues," Cancer Res. **35**(5), 1164–1167 (1975).
[22]E. Rummeny, R. Weissleder, D. D. Stark, S. Saini, C. C. Compton, W. Bennett, P. F. Hahn, J. Wittenberg, R. A. Malt, and J. T. Ferrucci, "Primary liver tumors: Diagnosis by MR imaging," Am. J. Roentgenol. **152**(1), 63–72 (1989).
[23]H. Hatabu, D. C. Alsop, J. Listerud, M. Bonnet, and W. B. Gefter, "T_2^* and proton density measurement of normal human lung parenchyma using submillisecond echo time gradient echo magnetic resonance imaging," Eur. J. Radiol. **29**(3), 245–252 (1999).
[24]A. I. Saito, J. G. Li, C. Liu, K. R. Olivier, and J. F. Dempsey, "Accurate heterogeneous dose calculation for lung cancer patients without

high-resolution CT densities," J. Appl. Clin. Med. Phys. **10**(2), 92–103 (2009).

[25]P. A. Bottomley, C. J. Hardy, R. E. Argersinger, and G. Allen-Moore, "A review of ^{1}H nuclear magnetic resonance relaxation in pathology: Are T_1 and T_2 diagnostic?," Med. Phys. **14**(1), 1–37 (1987).

[26]G. Held, F. Noack, V. Pollak, and B. Melton, "Proton spin relaxation and mobility of water in muscle tissue (author's transl)," Z. Naturforsch., C: Biochem., Biophys., Biol., Virol. **28**(1), 59–62 (1973).

[27]E. M. Haacke, R. W. Brown, M. R. Thompson, and R. Venkatesan, *Magnetic Resonance Imaging: Physical Principles and Sequence Design* (Wiley-Liss, New York, NY, 1999).

[28]C. A. Van den Berg, B. Van den Bergen, J. B. Van de Kamer, B. W. Raaymakers, H. Kroeze, L. W. Bartels, and J. J. Lagendijk, "Simultaneous B_1^+ homogenization and specific absorption rate hotspot suppression using a magnetic resonance phased array transmit coil," Magn. Reson. Med. **57**(3), 577–586 (2007).